

1897 **Chapter 9**
1898 **Weak Focusing Synchrotron**

1899 **Abstract** This Chapter introduces to the weak focusing synchrotron, and to the the-
1900 oretical material needed for the simulation exercises. It begins with a brief reminder
1901 of the historical context, and continues with beam optics and acceleration techniques
1902 which the weak focusing synchrotron principle and methods lean on. Regarding the
1903 latter, it relies on basic charged particle optics and acceleration concepts introduced
1904 in the previous Chapters, and further addresses the following aspects:

- 1905 - fixed closed orbit,
- 1906 - periodic structure,
- 1907 - periodic motion stability,
- 1908 - optical functions,
- 1909 - synchrotron motion,
- 1910 - depolarizing resonances.

1911 The simulation of a weak focusing synchrotron lattice only requires two optical
1912 elements: DIPOLE or BEND to simulate combined function dipoles, and DRIFT to
1913 simulate straight sections. A third element CAVITE, is required for acceleration. Par-
1914 ticle monitoring requires keywords introduced in the previous Chapters, including
1915 FAISCEAU, FAISTORE, possibly PICKUPS, and some others. Spin motion com-
1916 putation and monitoring resort to SPNTRK, SPNPRT, FAISTORE. Optics matching
1917 and optimization use FIT[2]. INCLUDE is used, mostly here in order to shorten the
1918 input data files. SYSTEM is used to, mostly, resort to gnuplot so as to end simu-
1919 laitons with some specific graphs obtained by reading data from output files such as
1920 zgoubi.fai (resulting from the use of FAISTORE), zgoubi.plt (resulting from IL=2),
1921 or other zgoubi.*.out files resulting from a PRINT command.

1922 **Notations used in the Text**

$B; \mathbf{B}, B_{x,y,s}$	field value; field vector, its components in the moving frame
$B\rho = p/q; B\rho_0$	particle rigidity; reference rigidity
$C; C_0$	orbit length, $C = 2\pi R + \left[\begin{array}{l} \text{straight} \\ \text{sections} \end{array} \right]$; reference, $C_0 = C(p = p_0)$
E	particle energy
EFB	Effective Field Boundary
$f_{\text{rev}}, f_{\text{rf}}$	revolution and accelerating voltage frequencies
h	RF harmonic number, $h = f_{\text{rf}}/f_{\text{rev}}$
$m; m_0; M$	mass, $m = \gamma m_0$; rest mass; in units of MeV/c ²
$n = \frac{\rho}{B} \frac{dB}{d\rho}$	focusing index
$\mathbf{p}; p; p_0$	momentum vector; its modulus; reference
P_i, P_f	beam polarization, initial, final
q	particle charge
r, R	orbital radius; average radius, $R = C/2\pi$
s	path variable
v	particle velocity
$V(t); \hat{V}$	oscillating voltage; its peak value
x, x', y, y'	horizontal and vertical coordinates in the moving frame

1923

α	momentum compaction
α	trajectory angle
$\beta = v/c; \beta_0; \beta_s$	normalized particle velocity; reference; synchronous
β_u	betatron functions ($u : x, y$)
$\gamma = E/m_0$	Lorentz relativistic factor
δp	momentum offset or Dirac distribution
Δp	momentum offset
ε	wedge angle
ε_u	Courant-Snyder invariant ($u : x, r, y, l$, etc.)
ε_R	strength of a depolarizing resonance
μ_u	betatron phase advance, $\mu_u = \int_{\text{period}} ds/\beta_u(s)$ ($u : x, y$)
ν_u	wave numbers, radial, vertical, synchrotron ($u : x, y, s$)
ν_{sp}	spin tune
ρ, ρ_0	curvature radius; reference
σ	beam matrix
$\phi; \phi_s$	particle phase at voltage gap; synchronous phase
ϕ_u	betatron phase advance, $\phi_u = \int ds/\beta_u$ ($u : x, y$)
φ	spin angle to the vertical axis

1924 9.1 Introduction

1925 The synchrotron is an outcome of the mid-1940s longitudinal phase focusing syn-
 1926 chronous acceleration concept [1, 2]. In its early version, transverse beam stability
 1927 in the synchrotron during the thousands of turns that the acceleration lasts was based
 1928 on the technique known at the time: weak focusing, as in the cyclotron and in the be-
 1929 tratron. An existing betatron was used to first demonstrate phase-stable synchronous
 1930 acceleration with slow variation of the magnetic field, on a fixed orbit, in 1946 [3],
 1931 - closely following the demonstration of the principle of phase focusing using a
 1932 fixed-field cyclotron [4].

1933 Phase focusing states that stability of the longitudinal motion, longitudinal focus-
 1934 ing, is obtained if particles in a bunch, which have a natural energy spread, arrive
 1935 at the accelerating gap in the vicinity of a proper phase of the oscillating voltage,
 1936 the synchronous phase; if this condition is fulfilled the bunch stays together, in the
 1937 vicinity of the latter, during acceleration. Synchrotrons operate in general in a non-
 1938 isochronous regime: the revolution period changes with energy; as a consequence,
 1939 in order to maintain an accelerated bunch on the synchronous phase, the RF voltage
 1940 frequency, which satisfies $f_{rf} = h f_{rev}$, has to change continuously from injection to
 1941 top energy. The reference orbit in a synchrotron is maintained at constant radius by
 1942 ramping the guiding field in the main dipoles in synchronism with the acceleration,
 1943 as in the betatron [5].

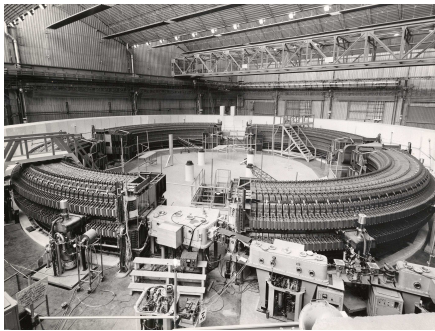


Fig. 9.1 SATURNEI at Saclay [6], a 3 GeV, 4-period, 68.9 m circumference, weak focusing synchrotron, constructed in 1956-58. The injection line can be seen in the foreground, injection is from a 3.6 MeV Van de Graaff (not visible)

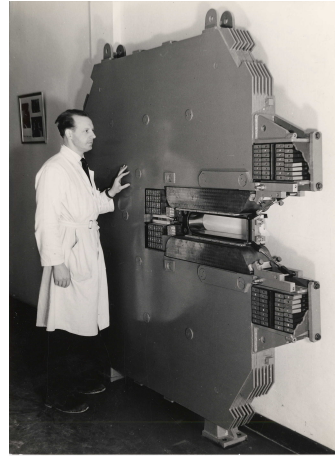


Fig. 9.2 A slice of SATURNEI dipole [6]. The slight gap tapering is hardly visible (increasing outward), it determines the weak index condition $0 < n < 1$

1944 The synchrotron concept allowed the highest energy reach by particle accelerators
 1945 at the time, it led to the construction of a series of proton rings with increasing
 1946 energy [7]: 1 GeV at Birmingham (1953), 3.3 GeV at the Cosmotron (Brookhaven

1947 National Laboratory, 1953-1969), 6.2 GeV at the Bevatron (Berkeley, 1954-1993),
 1948 10 GeV at the Synchro-Phasotron (JINR, Dubna, 1957-2003), and a few additional
 1949 ones in the late 1950s well into the era of the concept which would essentially
 1950 dethrone the weak focusing method and its quite bulky rings of magnets which were
 1951 a practical limit to further increase in energy¹: the strong focusing synchrotron (the
 1952 object of Chapter 10). The general layout of these first weak focusing synchrotrons
 1953 included straight sections (often 4, Fig. 9.1), which allowed insertion of injection
 1954 (Fig. 9.1) and extraction systems, accelerating cavities, orbit correction and beam
 1955 monitoring equipment.

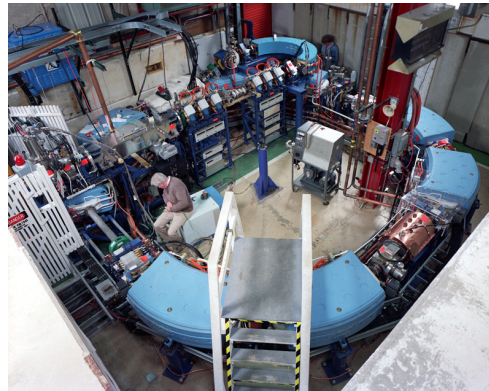


Fig. 9.3 Left: Loma Linda University medical synchrotron [8], during commissioning in 1989 at the Fermilab National Laboratory where it was designed

1956 The next decades following the invention of the synchrotron saw applications in
 1957 many fields of science including fixed-target nuclear physics for particle discovery,
 1958 material science, medicine, industry. Its technological simplicity still makes it an
 1959 appropriate technology today in low energy beam application when relatively low
 1960 current is not a concern, as in the hadrontherapy application (Fig. 9.3) [9, 10]: it
 1961 essentially requires a single type of a simple dipole magnet, an accelerating gap, some
 1962 command-control instrumentation, whereas it procures greater beam manipulation
 1963 flexibilities compared to (synchro-)cyclotrons.

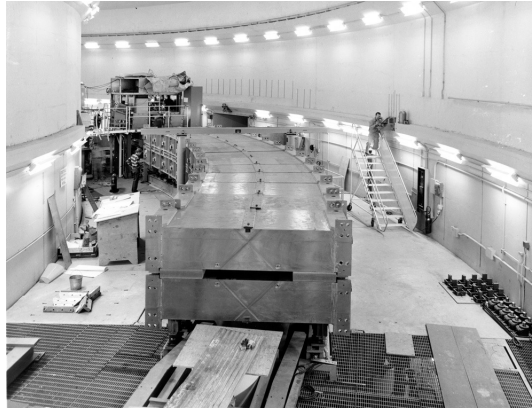
1964 *Polarized beams*

1965 The availability of polarized proton sources allowed the acceleration of polarized
 1966 beams to high energy. The possibility was considered from the early times at Argonne
 1967 ZGS (Zero-Gradient Synchrotron), a 12 GeV weak focusing synchrotron operated
 1968 over 1964-1979 [11] (Fig. 9.4). Up to 70% polarization transmission through the syn-
 1969 chrotron was achieved, for the first time in a synchrotron² and reaching multi-GeV

¹ The story has it that it is possible to ride a bicycle in the vacuum chamber of Dubna's Synchro-Phasotron.

² Polarized beam had been accelerated in cyclotrons, at earlier times.

Fig. 9.4 The ZGS at Argonne during construction. A 12 GeV, 8-dipole, 4-period, 172 m circumference, wedge focusing synchrotron. The two persons inside and outside the ring, in the background, give an idea of the size of the magnets



1970 energy in 1973, up to 17.5 GeV/c with *appreciable polarizations* [12]. Polariza-
 1971 tion preservation techniques included harmonic orbit correction and fast betatron
 1972 tune jump at strongest depolarizing resonances [13] (Fig. 9.16). Experiments were
 1973 performed to assess the possibility of polarization transmission in strong focusing
 1974 synchrotrons, and polarization lifetime in colliders [14]. Acceleration of polarized
 1975 deuteron was achieved in the late 1970s, when sources were made available [15].

1976 9.2 Basic Concepts and Formulae

1977 The synchrotron is based on two key principles. On the one hand, a slowly varying
 1978 magnetic field to maintain a constant orbit during acceleration,

$$B(t) \times \rho = p(t)/q, \quad \rho = \text{constant}, \quad (9.1)$$

1979 with $p(t)$ the particle momentum and ρ the bending radius in the dipoles. On the other
 1980 hand, on synchronous acceleration for longitudinal phase stability. In a regime where
 1981 the velocity change with energy cannot be ignored (non-ultrarelativistic particles),
 1982 the latter requires a modulation of the accelerating voltage frequency so to satisfy

$$f_{rf}(t) = h f_{rev}(t) \quad (9.2)$$

1983 Synchronism between accelerating voltage oscillation and the revolution motion
 1984 keeps the bunch on the synchronous phase at traversal of the accelerating gaps.
 1985 Synchronous acceleration is technologically simpler in the case of electrons, as
 1986 frequency modulation is unnecessary beyond a few MeV; for instance, from $v/c =$
 1987 0.9987 at 10 MeV to $v/c \rightarrow 1$ the relative change in revolution frequency amounts
 1988 to $\delta f_{rev}/f_{rev} = \delta\beta/\beta < 0.0013$.

1989 These are two major evolutions compared to the cyclotron, where, instead, the
 1990 magnetic field is fixed - the reference orbit spirals out, and, by virtue of the isochro-
 1991 nism of the orbits, the oscillating voltage frequency is fixed as well.

1992 A fixed orbit reduces the radial extent of individual guiding magnets, allowing a
 1993 ring structure comprised of a circular string of dipoles. For the sake of comparison:
 1994 a synchrocyclotron instead uses a single, massive dipole; increased energy requires
 1995 increased radial extent of the magnet to allow for the greater bending field integral
 1996 (*i.e.*, $\oint B dl = 2\pi R_{\max} \hat{B} = p_{\max}/q$), thus a volume of iron increasing more than
 1997 quadratically with bunch rigidity.

1998 One or the other of the weak index ($-1 < k < 0$, Sect. 4.2.2) and/or wedge
 1999 focusing (Sect. 15.3.1) are used in weak focusing synchrotrons. Transverse stability
 2000 was based on the latter at Argonne ZGS (Zero-Gradient Synchrotron: the main
 2001 magnet had no field index); ZGS accelerated polarized proton beams, weak focusing
 2002 resulted in weak depolarizing resonances, an advantage in that matter [14].

2003 Due to the necessary ramping of the field, and of the RF frequency to follow,
 2004 in order to maintain a constant orbit, the synchrotron is a pulsed accelerator, the
 2005 acceleration is cycled, from injection to top energy, repeatedly. The repetition rate
 2006 of the acceleration cycle depends on the type of power supply. If the ramping uses a
 2007 constant electromotive force ($E=V+ZI$ is constant), then

$$B(t) \propto (1 - e^{-t/\tau}) = 1 - \left[1 - \left(\frac{t}{\tau}\right) + \left(\frac{t}{\tau}\right)^2 - \dots \right] \approx \frac{t}{\tau} \quad (9.3)$$

2008 essentially linear; $\dot{B} = dB/dt$ does not exceed a few Tesla/second: the repetition rate
 2009 of the acceleration cycle if of the order of a Hertz. If instead the magnet winding
 2010 is part of a resonant circuit then the field oscillates from an injection threshold to a
 2011 maximum value, $B(t) : B_0 \rightarrow B_0 + \hat{B}$, as in the betatron; the repetition rate is up to
 2012 a few tens of Hertz. In both cases anyway B imposes its law and the other quantities
 2013 comprising the acceleration cycle (RF frequency in particular) will follow B(t).

2014 For the sake of comparison: in a synchrocyclotron the field is constant, thus
 2015 acceleration can be cycled as fast as the swing of the voltage frequency allows
 2016 (hundreds of Hz are common practice); assume a conservative 10 kVolts per turn,
 2017 thus of the order of 10,000 turns to 100 MeV, with velocity $0.046 < v/c < 0.43$
 2018 from 1 to 100 MeV, proton. Take $v \approx 0.5c$ to make it simple, an orbit circumference
 2019 below 30 meter, thus the acceleration takes of the order of $10^4 \times C/0.5c \approx \text{ms}$ range,
 2020 potentially a repetition rate in kHz range, more than an order of magnitude beyond
 2021 the reach of a rapid-cycling pulsed synchrotron.

2022 9.2.1 Periodic Stability

2023 This section introduces the various components of the transverse focusing and the
 2024 conditions for periodic stability in a weak focusing synchrotron. It builds on material
 2025 introduced in Chap. 4, Classical Cyclotron.

2026 **9.2.1.1 Closed orbit**

2027 The concept is found in the betatron, which accelerates particles on a constant orbit
 2028 (Chap. 7). The closed orbit is fixed, and maintained during acceleration by ensuring
 2029 that the relationship Eq. 9.1 is satisfied. In a perfect ring, the closed orbit is along an
 2030 arc in the bending magnets and straight along the drifts, Fig. 9.5.

2031 Particle motion is defined in a moving frame (O;s,x,y) whose origin coincides
 2032 with the location of an ideal particle following the reference orbit. The moving frame
 2033 *s* axis is tangent to the reference orbit, its transverse horizontal axis *x* is normal to
 2034 the *s* axis, its vertical axis *y* is normal to the (*s*, *x*) plane (Fig. 4.8, Sect. 4.2.2).

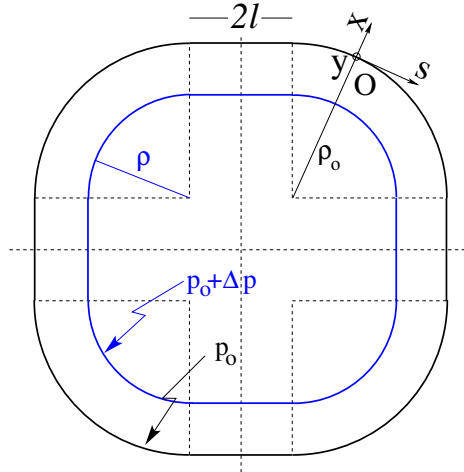


Fig. 9.5 A $2\pi/4$ axially symmetric structure with four drift spaces. Orbit length on reference momentum p_0 is $C = 2\pi\rho_0 + 8l$. (O;s,x,y) is the moving frame, along the reference orbit. The orbit for momentum $p = p_0 + \Delta p$ ($\Delta p < 0$, here) is at constant distance $\Delta x = \frac{\rho_0}{1-n} \frac{\Delta p}{p_0} = \frac{R}{(1+k)(1-n)} \frac{\Delta p}{p_0}$ from the reference orbit

2035 **9.2.1.2 Transverse Focusing**

2036 Radial motion stability around a reference closed orbit in an axially symmetric dipole
 2037 field requires a field index (Sect. 4.2.2),

$$n = -\frac{\rho_0}{B_0} \left. \frac{\partial B_y}{\partial x} \right|_{x=0, y=0} \quad (9.4)$$

2038 a quantity evaluated on the reference arc in the dipoles, satisfying the weak focusing
 2039 condition (Eq. 4.11 with $n = -k$)

$$0 < n < 1 \quad (9.5)$$

2040 This condition can be obtained with a tapered gap (as in SATURNE dipoles, Fig. 9.2)
 2041 causing the magnetic field to decrease slowly with radius, so resulting in both axial

2042 and radial focusing (Figs. 9.6, 9.7). Note the sign convention here, the cyclotron uses
 2043 the opposite sign (Eq. 4.10). This condition holds regardless of the presence of drifts
 2044 or not. Adding drift spaces between the dipoles, the reference orbit is comprised of
 2045 arcs of radius ρ_0 in the magnets, and straight segments along the drift spaces that
 2046 connect these arcs. This requires defining two radii, namely,

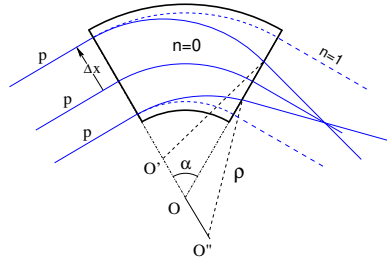


Fig. 9.6 Geometrical focusing: in a sector dipole with focusing index $n = 0$, parallel incoming rays of equal momenta experience the same curvature radius ρ , their trajectories converge as outer trajectories have a longer path in the field, inner ones shorter. An index value $n=1$ cancels that effect: parallel incoming rays exit parallel

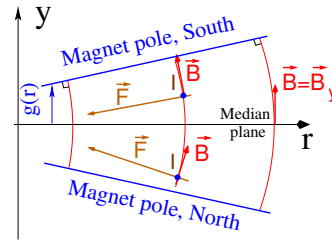


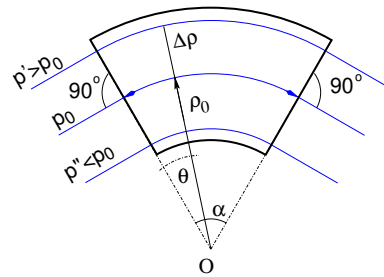
Fig. 9.7 Axial motion stability requires proper shaping of field lines: B_y has to decrease with radius. The Laplace force pulls a positive charge with velocity pointing out of the page, at I, toward the median plane. Increasing the field gradient (n closer to 1, gap opening up faster) increases the focusing

2047 (i) the magnet curvature radius ρ_0 ,
 2048 (ii) an average radius $R = C/2\pi = \rho_0 + Nl/\pi$ (with C the length of the reference
 2049 closed orbit and $2l$ the drift length) (Fig. 9.5) which also writes

$$R = \rho_0(1 + k), \quad k = \frac{Nl}{\pi\rho_0} \quad (9.6)$$

2050 Adding drift spaces decreases the average focusing around the ring.

Fig. 9.8 In a sector dipole with radial index $n \neq 0$, closed orbits follow arcs of constant field. A closed orbit at $p_0 + \Delta p$ follows an arc of radius $\rho_0 + \Delta\rho$, $\Delta\rho = \Delta p / (1 + n)qB_0$



2051 *Geometrical focusing*

2052 The limit $n \rightarrow 1$ of the transverse motion stability domain corresponds to a cancel-
 2053 lation of the geometrical focusing (Fig. 9.6): in a constant field dipole (radial field
 2054 index $n=0$) the longer (respectively shorter) path in the magnetic field for parallel
 2055 trajectories entering the magnet at greater (respectively smaller) radius result in
 2056 convergence. This effect is cancelled, *i.e.*, trajectory angle is the same whatever the
 2057 entrance radius, if the curvature center is made independent of the entrance radius:
 2058 $OO' = 0, O''O = 0$. This occurs if trajectories at an outer (inner) radius experience a
 2059 smaller (greater) field such as to satisfy $BL = B\rho\alpha = C^{st}$. Differentiating $B\rho = C^{st}$
 2060 gives $\frac{\Delta B}{B} + \frac{\Delta\rho}{\rho} = 0$, with $\Delta\rho = \Delta x$, so yielding $n = -\frac{\rho_0}{B_0} \frac{\Delta B}{\Delta x} = 1$. The focal distance
 2061 associated with the curvature is (Eq. 4.12 with $R = \rho_0$) $f = \frac{\rho_0^2}{L}$. Optical drawbacks
 2062 of the weak focusing method include the weakness of the focusing and the absence
 2063 of independent radial and axial focusing.

2064 *Wedge Focusing*

2065 Entrance and exit wedge angles may be used to ensure transverse focusing, Fig. 9.9:
 2066 opening the magnetic sector increases the horizontal focusing (and decreases the
 2067 vertical focusing); closing the magnetic sector has the reverse effect (see Sect. 15.3.1).

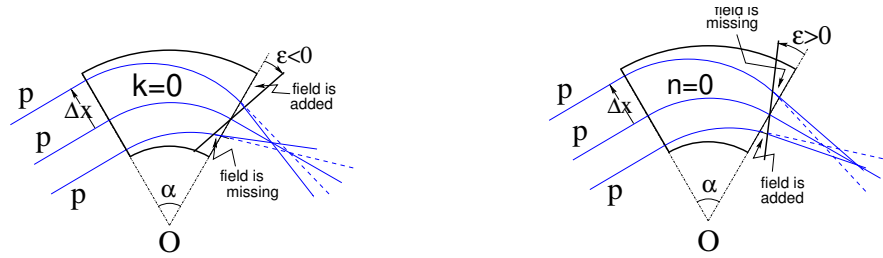


Fig. 9.9 Left: a focusing wedge ($\epsilon < 0$); opening the sector increases horizontal focusing and decreases vertical focusing. Right: a defocusing wedge ($\epsilon > 0$), closing the sector, has the reverse effect. This is the origin of the focusing in the ZGS zero-gradient dipoles

2068 In a point transform approximation, at the wedge the trajectory undergoes a local
 2069 deviation proportional to the distance to the optical axis, amounting to

$$\Delta x' = \frac{\tan \epsilon}{\rho_0} \Delta x, \quad \Delta y' = -\frac{\tan(\epsilon - \psi)}{\rho_0} \Delta y \quad (9.7)$$

2070 The ψ angle component is a correction for the fringe field extent (Eq. 15.21); the
 2071 effect of the latter, of the first order on the vertical focusing, is of second order
 2072 horizontally.

2073 Profiling the magnet gap in order to adjust the focal distance complicates the
 2074 magnet; a parallel gap, $n = 0$, makes it simpler, for that reason edge focusing may
 2075 be preferred. Wedge vertical focusing in the ZGS ($\varepsilon > 0$) was at the expense of
 2076 horizontal geometrical focusing (Fig. 9.6). This was an advantage though, for the
 2077 acceleration of polarized beams, as radial field components (which are responsible for
 2078 depolarization) were only met at the EFBs of the eight main dipoles, and weak [12].
 2079 Preserving beam polarization at high energy required tight control of the tunes, this
 2080 was achieved by pole face windings added at the ends of the dipoles [16, 17], pulsed
 2081 to control the amplitude detuning, resulting in a control of the tunes at 0.01 level.

2082 9.2.1.3 Betatron motion

2083 The first order differential equations of motion in the moving frame (Fig. 9.5) derive
 2084 from the Lorentz equation

$$\frac{dm\mathbf{v}}{dt} = q\mathbf{v} \times \mathbf{B} \Rightarrow m \frac{d}{dt} \begin{pmatrix} \frac{ds}{dt} \mathbf{s} \\ \frac{dx}{dt} \mathbf{x} \\ \frac{dy}{dt} \mathbf{y} \end{pmatrix} = q \begin{pmatrix} \left(\frac{dx}{dt} B_y - \frac{dy}{dt} B_x \right) \mathbf{s} \\ -\frac{ds}{dt} B_y \mathbf{x} \\ \frac{ds}{dt} B_x \mathbf{y} \end{pmatrix} \quad (9.8)$$

2085 Motion in a weak index dipole field is solved in Sect. 4.2.2, Classical Cyclotron: in
 2086 the latter substitute ρ to R , $n = -\frac{\rho_0}{B_0} \frac{\partial B_y}{\partial x}$ to $-k$, evaluated on the reference orbit.
 2087 Taylor expansions of the transverse field components in the moving frame (Eq. 4.6)
 2088 lead to

$$\begin{aligned} B_y(\rho)|_{y=0} &= B_0(1 - n \frac{x}{\rho_0}) + \mathcal{O}(x^2) \\ B_x(0 + y) &= -n \frac{B_0}{\rho_0} y + \mathcal{O}(y^3) \end{aligned} \quad (9.9)$$

2089 Assume transverse stability: $0 < n < 1$; in the approximation $ds \approx vdt$ (Eq. 4.13)
 2090 Eqs. 9.8, 9.9 lead to the differential equations of motion

$$\frac{d^2x}{ds^2} + \frac{1-n}{\rho_0^2} x = 0, \quad \frac{d^2y}{ds^2} + \frac{n}{\rho_0^2} y = 0 \quad (9.10)$$

2091 It results that, in an S-periodic structure comprised of gradient dipoles, wedges
 2092 and drift spaces, the differential equation of motion takes the general form of Hill's
 2093 equation, a second order differential equation with periodic coefficient, namely (with
 2094 u standing for x or y),

$$\begin{cases} \frac{d^2u}{ds^2} + K_u(s)u = 0 \\ K_u(s+S) = K_u(s) \end{cases} \quad \text{with} \quad \begin{cases} \text{in dipoles : } \begin{cases} K_x = \frac{1-n}{\rho_0^2} \\ K_y = \frac{n}{\rho_0^2} \end{cases} \\ \text{at a wedge at } s = s_0 : K_x = \frac{\pm \tan \varepsilon}{\rho_0} \delta(s - s_0) \\ \text{in drift spaces : } \frac{1}{\rho_0} = 0, K_x = K_y = 0 \end{cases} \quad (9.11)$$

2095 $K_u(s)$ is S-periodic, $S = 2\pi R/N$ ($S = C/4$ for instance in a 4-periodic ring,
2096 Figs. 9.1, 9.5).

2097 The solution of Eqs. 9.11 is not as straightforward as in the cyclotron where K_u is
2098 constant around the ring (Eq. 4.14), which results in a sinusoidal motion (Eq. 4.16)
2099 - the latter is on the other hand a reasonable approximation, see below, *Weak focusing*
2100 *approximation*. G. Floquet has established [18] that the two independent solutions
2101 of Hill's second order differential equation have the form [19]

$$\left\{ \begin{array}{l} u_1(s) = \sqrt{\beta_u(s)} e^{i \int_0^s \frac{ds}{\beta_u(s)}} \\ du_1(s)/ds = \frac{i - \alpha_u(s)}{\beta_u(s)} u_1(s) \end{array} \right. \quad \text{and} \quad \left\{ \begin{array}{l} u_2(s) = u_1^*(s) \\ du_2(s)/ds = du_1^*(s)/ds \end{array} \right. \quad (9.12)$$

2102 wherein $\beta_u(s)$ and $\alpha_u(s) = -\beta'_u(s)/2$ are S-periodic functions, from what it results
2103 that

$$u_{\frac{1}{2}}(s + S) = u_{\frac{1}{2}}(s) e^{\pm i \mu_u} \quad (9.13)$$

2104 wherein

$$\mu_u = \int_{s_0}^s \frac{ds}{\beta_u(s)} \quad (9.14)$$

2105 is the betatron phase advance at s , from the origin s_0 . A real solution of Hill's
2106 equation is the linear combination $A u_1(s) + A^* u_2^*(s)$. With $A = \frac{1}{2} \sqrt{\varepsilon_u/\pi} e^{i\phi}$
2107 following conventional notations, ϕ the phase of the motion at the origin $s = s_0$, the
2108 general solution of Eq. 9.11 writes

$$\left\{ \begin{array}{l} u(s) = \sqrt{\beta_u(s)\varepsilon_u/\pi} \cos\left(\int_{s_0}^s \frac{ds}{\beta_u} + \phi\right) \\ u'(s) = -\sqrt{\frac{\varepsilon_u/\pi}{\beta_u(s)}} \sin\left(\int_{s_0}^s \frac{ds}{\beta_u} + \phi\right) + \alpha_u(s) \cos\left(\int_{s_0}^s \frac{ds}{\beta_u} + \phi\right) \end{array} \right. \quad (9.15)$$

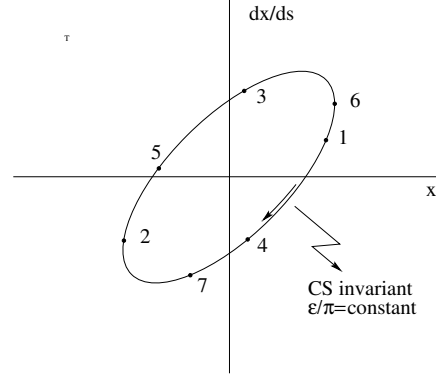
2109 An invariant of the motion, known as the Courant-Snyder invariant, is

$$\frac{1}{\beta_u(s)} \left[u^2 + (\alpha_u(s)u + \beta_u(s)u')^2 \right] = \frac{\varepsilon_u}{\pi} \quad (9.16)$$

2110 At a given azimuth s of the periodic structure the observed turn-by-turn motion
2111 lies on that ellipse (Fig. 9.10). The form and inclination of the ellipse depend on
2112 the observation azimuth s via the respective local values of $\alpha_u(s)$ and $\beta_u(s)$, but
2113 its surface ε_u is invariant. Motion along the ellipse is clockwise, as can be figured
2114 from Eq. 9.15 considering an observation azimuth s where the ellipse is upright,
2115 $\alpha_u(s) = 0$. The phase advance over a turn (from one position to the next on the
2116 ellipse, Fig. 9.10) in an N-periodic ring yields the wave number

$$\nu_u = N\mu_u = \int_{s_0}^{s_0+NS} \frac{ds}{\beta_u(s)} = N \int_{\text{period}} \frac{ds}{\beta_u(s)} \quad (9.17)$$

Fig. 9.10 Courant-Snyder invariant and turn-by-turn harmonic motion along the invariant, observed at some azimuth s . The form and tilt-angle of the ellipse depend on the observation azimuth s but its surface ε_u is invariant



2117 *Weak focusing approximation*

2118 In a cylindrically symmetric structure a sinusoidal motion is the exact solution of the
 2119 first order differential equations of motion (Eqs. 4.15, 4.16, Classical Cyclotron Chap-
 2120 ter), the coefficients $K_x = (1 - n)/R_0^2$ and $K_y = n/R_0^2$ are constant (s -independent).
 2121 Adding drift spaces results in Hill's differential equation with periodic coefficient
 2122 $K(s+S) = K(s)$ (Eq. 9.11), and in a pseudo harmonic solution (Eq. 9.15). Due to the
 2123 weak focusing the beam envelope is only weakly modulated (see below), thus so is
 2124 $\beta_u(s)$. In a practical manner, the modulation of $\beta_u(s)$ does not exceed a few percent,
 2125 this justifies introducing the average value $\bar{\beta}_u$ to approximate the phase advance by

$$\int_0^s \frac{ds}{\beta_u(s)} \approx \frac{s}{\bar{\beta}_u} = \nu_u \frac{s}{R} \quad (9.18)$$

2126 The right equality is obtained by applying this approximation to the phase advance
 2127 per period, namely (Eq. 9.14) $\mu_u = \int_{s_0}^{s_0+S} \frac{ds}{\beta_u(s)} \approx S/\bar{\beta}_u$, and introducing the wave
 2128 number of the N -period optical structure $\nu_u = \frac{N\mu_u}{2\pi} = \frac{\text{phase advance over a turn}}{2\pi}$ so that

$$\bar{\beta}_u = \frac{R}{\nu_u} \quad (9.19)$$

2129 the wavelength of the betatron oscillation around the ring. With $k \ll 1$ and using
 2130 Eq. 9.23,

$$\bar{\beta}_x = \frac{\rho_0(1 + k/2)}{\sqrt{1 - n}}, \quad \bar{\beta}_y = \frac{\rho_0(1 + k/2)}{\sqrt{n}} \quad (9.20)$$

2131 Substituting $\nu_u \frac{s}{R}$ to $\int \frac{ds}{\beta_u(s)}$ in Eq. 9.15 yields the approximate solution

$$\begin{cases} u(s) \approx \sqrt{\beta_u(s)\varepsilon_u/\pi} \cos\left(\nu_u \frac{s}{R} + \phi\right) \\ u'(s) \approx -\sqrt{\frac{\varepsilon_u/\pi}{\beta_u(s)}} \sin\left(\nu_u \frac{s}{R} + \phi\right) + \alpha_u(s) \cos\left(\nu_u \frac{s}{R} + \phi\right) \end{cases} \quad (9.21)$$

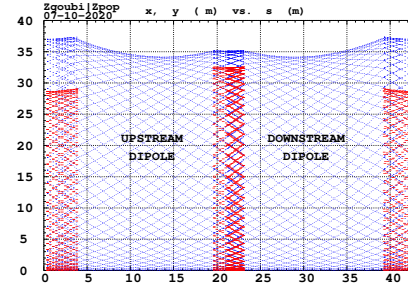
2132 *Beam envelopes*

2133 The beam envelope $\hat{u}(s)$ (with u standing for x or y) is determined by the particle of
 2134 maximum invariant ε_u/π , it is given at all s by

$$\hat{u}_{\text{env}}(s) = \pm \sqrt{\beta_u(s) \frac{\varepsilon_u}{\pi}} \quad (9.22)$$

As $\beta_u(s)$ is S -periodic, so is the envelope, $\hat{u}(s+S) = \hat{u}(s)$. In a cell with symmetries,

Fig. 9.11 Multi-turn particle excursion along the ZGS 2-dipole 43 m cell. The motion extrema (Eq. 9.22) tangent the envelopes, respectively horizontal (red), and vertical (blue). Envelops have the symmetry of the cell



2135 beam envelopes feature the same symmetries, as in Fig. 9.11 for instance: a symmetry
 2136 with respect to the center of the cell; envelop extrema are at azimuth s of $\beta_u(s)$
 2137 extrema, *i.e.* where $d\hat{u}(s)/ds \propto \beta'_u(s) = 0$ or $\alpha_u = 0$ as $\beta'_u = -2\alpha_u$.
 2138

2139 *Working point*

2140 The “working point” of the synchrotron is the wave number couple (ν_x, ν_y) at which
 2141 the accelerator is operated, it fully characterizes the focusing. In a structure with
 2142 cylindrical symmetry (such as the Classical Cyclotron) $\nu_x = \sqrt{1-n}$ and $\nu_y = \sqrt{n}$
 2143 (Eq. 4.17) so that $\nu_x^2 + \nu_y^2 = 1$: when the radial field index n is changed the working
 2144 point stays on a circle of radius 1 in the stability diagram (or “tune diagram”,
 2145 Fig. 9.12). If drift spaces are added, from Eqs. 9.19, 9.20, with $1 + \frac{k}{2} \approx \sqrt{R/\rho_0}$
 2146 (Eq. 9.6), it comes

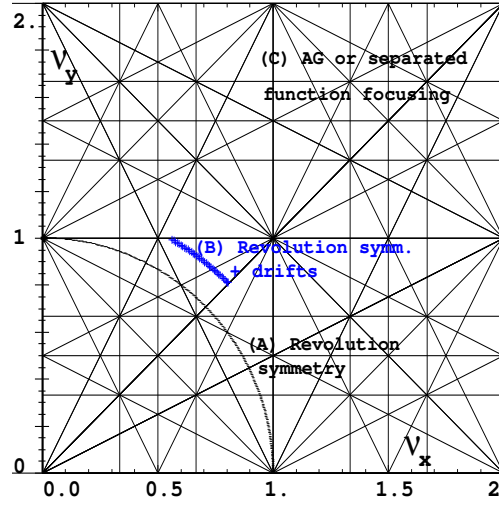
$$\nu_x \approx \sqrt{(1-n) \frac{R}{\rho_0}}, \quad \nu_y \approx \sqrt{n \frac{R}{\rho_0}}, \quad \nu_x^2 + \nu_y^2 \approx \frac{R}{\rho_0} \quad (9.23)$$

thus the working point is located on the circle of radius $\sqrt{R/\rho_0} > 1$ (Fig. 9.12), tunes
 can not exceed the limits

$$0 < \nu_{x,y} \lesssim \sqrt{R/\rho_0}$$

2147 Horizontal and vertical focusing are not independent (Eq. 9.11): if ν_x increases then
 2148 ν_y decreases and reciprocally. This is a lack of flexibility which the advent of strong

Fig. 9.12 Location of the working point in the tune diagram. (A) field with revolution symmetry: (ν_x, ν_y) is on a circle of radius 1; (B) sector field with index $0 < n < 1$ and drift spaces: (ν_x, ν_y) is on a circle of radius $(\sqrt{R/\rho_0})$; (C) strong focusing, AG index $|n| \gg 1$ or separated function, ν_x and ν_y are large, set independently



2149 focusing will overcome by providing two knobs allowing separate adjustment of the
2150 tunes.

2151 *Off-momentum orbits; periodic dispersion*

2152 In the linear approximation in $\Delta p/p_0$, a momentum offset $\Delta p = p - p_0$ changes mv to
2153 $mv(1 + \Delta p/p_0)$ in Eq. 9.8; this changes the horizontal equation of motion (Eq. 9.10)
2154 to

$$\frac{d^2x}{ds^2} + K_x x = \frac{1}{\rho_0} \frac{\Delta p}{p_0}, \quad \text{or} \quad \frac{d^2x}{ds^2} + K_x \left(x - \frac{1}{\rho_0 K_x} \frac{\Delta p}{p_0} \right) = 0 \quad (9.24)$$

2155 A change of variable $x - \frac{1}{K_x \rho_0} \frac{\Delta p}{p_0} \rightarrow x$ (with $1/\rho_0 K_x = \rho_0/(1-n)$) restores the
2156 unperturbed equation of motion; thus orbits of different momenta $p = p_0 + \Delta p$ are
2157 distant

$$\Delta x = \frac{\rho_0}{1-n} \frac{\Delta p}{p_0} \quad (9.25)$$

2158 from the reference orbit (Fig. 9.8). Introduce the geometrical radius $R = (1+k)\rho_0$
2159 (Eq. 9.6) to account for the added drifts; this yields the dispersion function

$$D_x = \frac{\Delta x}{\Delta p/p_0} \equiv \frac{\Delta R}{\Delta p/p_0} = \frac{R}{(1-n)(1+k)} = \frac{\rho_0}{1-n}, \quad \text{constant, positive} \quad (9.26)$$

2160 D_x is the chromatic dispersion of the orbits, an s -independent quantity: in a structure
2161 with axial symmetry, comprising drift sections (Fig. 9.5) or not (classical and AVF
2162 cyclotrons for instance), the ratio $\frac{\Delta x}{\rho_0 \Delta p/p_0}$ is independent of the azimuth s , the
2163 distance of a chromatic orbit to the reference orbit is constant around the ring.

- 2164 Given that $n < 1$,
 2165 - higher momentum orbits, $p > p_0$, have a greater radius,
 2166 - lower momentum orbits, $p < p_0$, have a smaller radius.

2167 The horizontal motion of an off-momentum particle is a superposition of the
 2168 betatron motion (solution of Hill's Eq. 9.21 with $\delta p/p = 0$) and of a particular
 2169 solution of the inhomogeneous equation ($\delta p/p \neq 0$), namely

$$x(s) = \sqrt{\beta_u(s)\epsilon_u/\pi} \cos\left(\nu_u \frac{s}{R} + \phi\right) + \frac{\rho_0}{1-n} \frac{\Delta p}{p_0} \quad (9.27)$$

2170 whereas the vertical motion is unchanged.

2171 *Chromatic orbit length*

2172 In an axially symmetric structure the difference in closed orbit length $\Delta C = 2\pi\Delta R$
 2173 resulting from the difference in momentum arises in the dipoles, as all orbits are
 2174 parallel in the drifts (Fig. 9.5). Hence, from Eq. 9.26, the relative closed orbit
 2175 lengthening factor, or momentum compaction

$$\alpha = \frac{\Delta C}{C} \Big/ \frac{\Delta p}{p_0} \equiv \frac{\Delta R}{R} \Big/ \frac{\Delta p}{p_0} = \frac{1}{(1-n)(1+k)} \approx \frac{1}{\nu_x^2} \quad (9.28)$$

2176 with $k = NI/\pi\rho_0$ (Eq. 9.6). Note that the relationship $\alpha \approx 1/\nu_x^2$ between momentum
 2177 compaction and horizontal wave number established for a revolution symmetry
 2178 structure (Eq. 4.21) still holds when adding drifts.

2179 **9.2.2 Acceleration**

In a synchrotron, the field B is varied during acceleration (a function performed by the magnet power supply) concurrently with the variation of the bunch momentum p (a function performed by the accelerating cavity) in such a way that the beam is maintained on the design orbit. Given the energies involved, the magnet supply imposes its law $B(t)$ (Fig. 9.13) and the cavity follows, the best it can. The accelerating voltage $\hat{V}(t) = \sin \omega_{\text{rf}} t$ is maintained in synchronism with the revolution motion, its angular frequency satisfying

$$\omega_{\text{rf}} = h\omega_{\text{rev}} = h \frac{c}{R} \frac{B(t)}{\sqrt{\left(\frac{m_0 c}{q\rho}\right)^2 + B^2(t)}}$$

Typically, for a $C = 2\pi R \approx 70$ m circumference ring (SATURNEI weak focusing synchrotron, Fig. 9.1; cf. Exercise 9.1, parameters in Tab. 9.1), from $\beta = v/c \approx 0.09$ at injection (3.6 MeV protons) to $\beta \approx 1$ at top energy (3 GeV), the revolution period

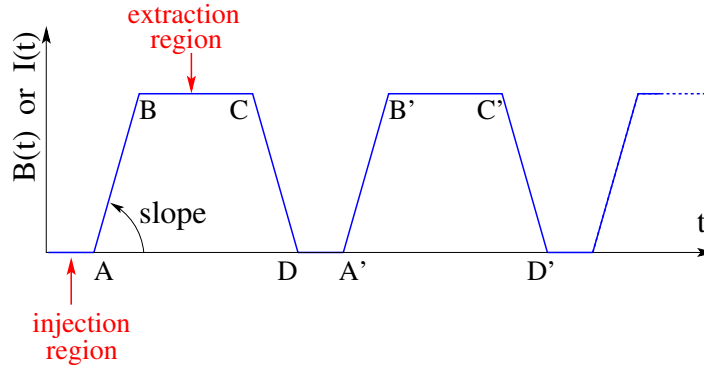


Fig. 9.13 Cycling $B(t)$ in a pulsed synchrotron. Ignoring saturation, $B(t)$ is proportional to the magnet power supply current $I(t)$. Beam injection occurs at low field, in the region of A, extraction occurs at top energy, on the high field plateau. (AB): field ramp up (acceleration); (BC): flat top; (CD): field ramp down; (DA'): thermal relaxation. (AA'): repetition period; $(1/AA')$: repetition rate; *slope*: ramp velocity $\dot{B} = dB/dt$ (Tesla/s).

$T_{\text{rev}} = C/\beta c$ and frequency $\omega_{\text{rev}}/2\pi = 1/T_{\text{rev}}$ span

$$\begin{cases} T_{\text{rev}} : 2.6 \mu\text{s} \rightarrow 23 \mu\text{s} \\ f_{\text{rev}} : 390 \text{ kHz} \rightarrow 4.3 \text{ MHz} \end{cases}$$

2180 *Energy gain*

2181 The variation of the particle energy over a turn amounts to the work of the force
2182 $F = dp/dt = q\rho dB/dt$ on the charge at the cavity, namely

$$\Delta W = F \times 2\pi R = 2\pi R q \rho \dot{B} \quad (9.29)$$

In a slow-cycling synchrotron \dot{B} is usually constant over most of the acceleration cycle (Eq. 9.3), thus so is ΔW . At SATURNE I for instance

$$\frac{\Delta W}{q} = 2\pi R \rho \dot{B} = 68.9 \times 8.42 \times 1.8 = 1044 \text{ volts}$$

The field ramp lasts

$$\Delta t = (B_{\text{max}} - B_{\text{min}})/\dot{B} \approx B_{\text{max}}/\dot{B} = 0.8 \text{ s}$$

The number of turns to the top energy ($W_{\text{max}} \approx 3 \text{ GeV}$) is

$$N = \frac{W_{\text{max}}}{\Delta W} = \frac{3 \cdot 10^9 \text{ eV}}{1044 \text{ eV/turn}} \approx 3 \cdot 10^6 \text{ turns}$$

The dependence of particle mass on field writes

$$m(t) = \gamma(t)m_0 = \frac{q\rho}{c} \sqrt{\left(\frac{m_0 c}{q\rho}\right)^2 + B(t)^2}$$

2183 *Adiabatic damping of the betatron oscillations*

Particle momentum increases at the accelerating gap, this results in a decrease of the amplitude of betatron oscillations (conversely, an increase if the cavity is decelerating). The mechanism is sketched in Fig. 9.14 (with u standing indifferently for the x or y coordinate): the slope, respectively before and after (index 2) the cavity is

$$\frac{du}{ds} = \frac{m \frac{du}{dt}}{m \frac{ds}{dt}} = \frac{p_u}{p_s}, \quad \frac{du}{ds} \Big|_2 = \frac{m \frac{du}{dt}}{m \frac{ds}{dt}} \Big|_2 = \frac{p_{u,2}}{p_{s,2}}$$

As the kick in momentum is longitudinal, $dp_u/dt = 0$ thus $p_{u,2} = p_u$, the increase

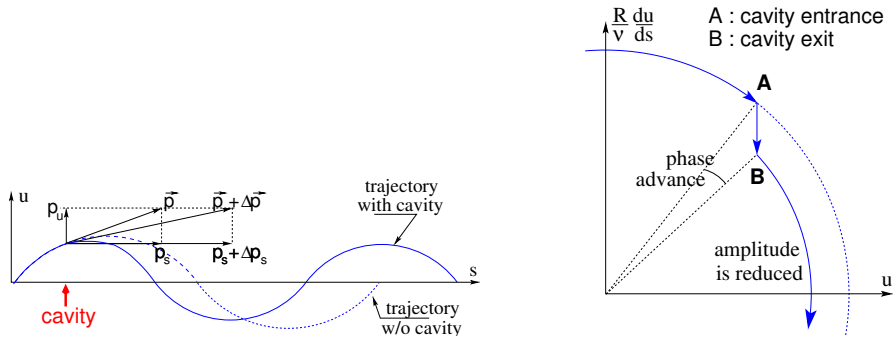


Fig. 9.14 Adiabatic damping of betatron oscillations, here from trajectory incidence $u' = p_u/p_s$ at cavity entrance, to $u'_2 = p_u/(p_s + \Delta p_s)$ at cavity exit. In the transverse phase space: decrease of the particle phase space invariant resulting from $\Delta \left(\frac{du}{ds} \right)$

in momentum is purely longitudinal, $p_{s,2} = p_s + \Delta p_s$. Thus

$$\frac{du}{ds} \Big|_2 = \frac{p_u}{p_s + \Delta p_s} \approx \frac{p_u}{p_s} \left(1 - \frac{\Delta p_s}{p_s} \right)$$

and as a consequence the slope du/ds varies across the cavity,

$$\Delta \left(\frac{du}{ds} \right) = \frac{du}{ds} \Big|_2 - \frac{du}{ds} = - \frac{du}{ds} \frac{\Delta p_s}{p_s}$$

2184 The variation of the slope is proportional to the slope, with opposite sign if $\Delta p/p > 0$
 2185 (acceleration) thus a decrease of the slope. This variation has two consequences on
 2186 the betatron oscillation (Fig. 9.14):

- 2187 - a change of the betatron phase,
 2188 - a modification of the betatron amplitude.

2189 *Coordinate transport*

2190 at the cavity writes $\begin{cases} u_2 = u \\ u'_2 \approx \frac{p_u}{p_s} (1 - \frac{dp}{p}) = u'(1 - \frac{dp}{p}) \end{cases}$. In matrix form, $\begin{pmatrix} u_2 \\ u'_2 \end{pmatrix} =$
 2191 $[C] \begin{pmatrix} u \\ u' \end{pmatrix}$ with

$$[C] = \begin{bmatrix} 1 & 0 \\ 0 & 1 - \frac{dp}{p} \end{bmatrix} \quad (9.30)$$

2192 and $\det[C] = 1 - \frac{dp}{p} \neq 1$: the system is non-conservative, the surface of the beam
 2193 ellipse in phase space is not conserved. Assume one cavity in the ring and note
 2194 $[T] \times [C]$ the one-turn coordinate transport matrix with origin at entrance of the
 2195 cavity. Its determinant is $\det[T] \times \det[C] = \det[C] = 1 - \frac{dp}{p}$; the variation of the
 2196 transverse ellipse surface satisfies $\varepsilon_u = (1 - \frac{dp}{p_0})\varepsilon_0$ or, with $d\varepsilon_u = \varepsilon_u - \varepsilon_0$, $\frac{d\varepsilon_u}{\varepsilon_u} = -\frac{dp}{p_0}$,
 2197 the solution of which is

$$p \varepsilon_u = \text{constant, or } \beta\gamma\varepsilon_u = \text{constant} \quad (9.31)$$

2198 Over N turns the coordinate transport matrix is $[T_N] = ([T][C])^N$, thus the ellipse
 2199 surface changes by a factor $\det[C]^N = (1 - \frac{dp}{p})^N \approx 1 - N\frac{dp}{p}$.

2200 *Phase stability*

2201 “Synchrotron motion” designates the mechanism of phase stability, or longitudinal
 2202 focusing (Fig. 9.15), that stabilizes the longitudinal motion of a particle in the vicinity
 2203 of a synchronous phase, ϕ_s , in virtue of

2204 (i) the presence of an accelerating cavity with its frequency indexed on the
 2205 revolution time,

2206 (ii) with the bunch centroid positioned either on the rising slope of the oscillating
 2207 voltage (low energy regime), or on the falling slope (high energy regime).

The synchronous (or “ideal”) particle follows the equilibrium trajectory around the ring (the reference closed orbit, about which all other particles will undergo a betatron oscillation), its velocity satisfies $v(t) = \frac{qB\rho(t)}{m}$; at each turn it reaches the accelerating gap when the oscillating voltage is at the synchronous phase ϕ_s , and undergoes an energy gain

$$\Delta W = q\hat{V} \sin \phi_s$$

The condition $|\sin \phi_s| < 1$ imposes a lower limit to the cavity voltage for acceleration to happen, namely, after Eq. 9.29,

$$\hat{V} > 2\pi R\rho\dot{B}$$

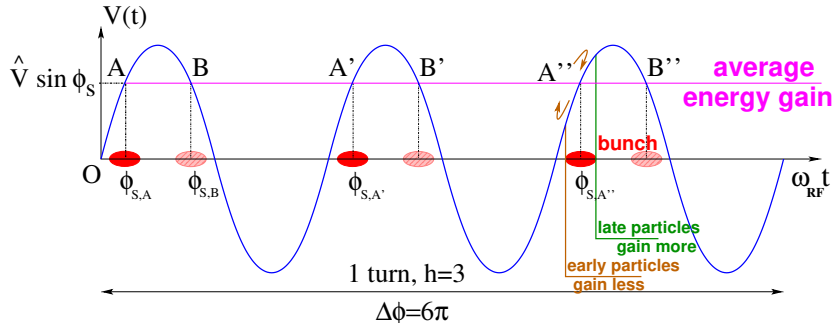


Fig. 9.15 A sketch of the mechanism of phase stability, $h = 3$ in this example. Below transition phase stability occurs for a synchronous phase taken at either of A, A', A'' arrival times at the gap: a particle with a little greater energy compared to the synchronous particle goes around the ring more rapidly than the latter: if both are launched together, the former arrives earlier at the voltage gap (at $\phi < \phi_{s,A}$) and thus experiences weaker acceleration; a particle with a little lower energy compared to the synchronous particle, is slower, it arrives at the gap later, $\phi > \phi_{s,A}$, and thus experiences greater voltage; in both cases the particle is pulled towards the synchronous phase, this results in an overall stable oscillatory motion around the synchronous phase. Beyond transition the stable phase is at either one of B, B', B'' locations: a particle which is less energetic than the synchronous particle arrives earlier, $\phi < \phi_{s,B}$, so experiencing a greater voltage, and inversely, resulting in overall stable synchrotron motion.

2208 Referring to Fig. 9.15, the synchronous phase can be placed on the left (A A' A''...
 2209 series in the Figure, or on the right (B B' B''... series) of the oscillating voltage crest.
 2210 One and only one of these two possibilities, and which one depending upon the optical
 2211 lattice and on particle energy, ensures that particles in a bunch remain grouped in
 2212 the vicinity of the synchronous particle. The transition is between two time-of-flight
 2213 regimes: a particle which gains momentum compared to the synchronous particle
 2214 has a greater velocity, while
 2215 - in the high bunch energy regime the increase in path length around the ring
 2216 is faster than the increase in velocity (velocity essentially does not even change
 2217 in ultrarelativistic regime), a revolution around the ring takes more time (this is the
 2218 classical cyclotron and synchrocyclotron regime, and as well the high energy electron
 2219 synchrotron regime); consider such a particle, arriving at the accelerating gap late
 2220 ($\phi(t) > \phi_s$), in order for it to be pulled toward bunch center (*i.e.*, take less time
 2221 around the ring) it has to undergo deceleration; this is the B series, above transition;
 2222 - in the low bunch energy regime velocity increase is faster than path length
 2223 increase, thus a revolution around the ring is faster; consider such a particle, arriving
 2224 at the accelerating gap early ($\phi(t) < \phi_s$), in order for it to be pulled toward bunch
 2225 center (*i.e.*, take more time around the ring) it has to be slowed down, it has to
 2226 undergo deceleration; this is the A series, below transition.

2227 *Transition energy*

2228 The transition between the two time-of-flight regimes occurs at $\frac{dT_{\text{rev}}}{T_{\text{rev}}} = 0$. With
 2229 $T = 2\pi/\omega = C/v$, this can be written $\frac{d\omega_{\text{rev}}}{\omega_{\text{rev}}} = -\frac{dT_{\text{rev}}}{T_{\text{rev}}} = \frac{dv}{v} - \frac{dC}{C}$. With $\frac{dv}{v} = \frac{1}{\gamma^2} \frac{dp}{p}$
 2230 and momentum compaction $\alpha = \frac{dC}{C} / \frac{dp}{p}$, (Eq. 9.28), this can be written

$$\frac{d\omega_{\text{rev}}}{\omega_{\text{rev}}} = -\frac{dT_{\text{rev}}}{T_{\text{rev}}} = \left(\frac{1}{\gamma^2} - \alpha \right) \frac{dp}{p} = \eta \frac{dp}{p} \quad (9.32)$$

2231 which introduces the phase-slip factor

$$\eta = \overbrace{\frac{1}{\gamma^2}}^{\text{kinematics}} - \underbrace{\alpha}_{\text{lattice}} = \frac{1}{\gamma^2} - \frac{1}{\gamma_{\text{tr}}^2} \quad (9.33)$$

2232 The transition γ_{tr} appears to be a property of the lattice.

2233 In a weak focusing lattice $\gamma_{\text{tr}} = 1/\sqrt{\alpha} \approx \nu_x$ (Eqs. 4.21, 9.28), thus the phase
 2234 stability regime is

$$\begin{aligned} &\text{below transition, i.e. } \phi_s < \pi/2, && \text{if } \gamma < \nu_x \\ &\text{above transition, i.e. } \phi_s > \pi/2, && \text{if } \gamma > \nu_x \end{aligned} \quad (9.34)$$

2235 In a weak focusing synchrotron the horizontal tune $\nu_x = \sqrt{(1-n)R/\rho_0}$ (Eq. 9.23)
 2236 may be ≥ 1 , and subsequently $\gamma_{\text{tr}} > 1$ is a possibility. There is no transition-gamma
 2237 if $\nu_x < 1$. At SATURNE I for instance, with $\nu_x \approx 0.7$ (Tab. 9.1) thus $\gamma_{\text{tr}} < 1$, ramping
 2238 in energy did not require transition-gamma crossing³.

2239 9.2.3 Depolarizing Resonances

2240 The field index is essentially zero in the ZGS, transverse focusing is ensured by
 2241 wedge angles at the ends of the height dipoles, the only location where non-zero
 2242 radial field components are found. The latter are weak, as a consequence so are
 2243 depolarizing resonances: “As we can see from the table, the transition probability
 2244 [from spin state $\psi_{1/2}$ to spin state $\psi_{-1/2}$] is reasonably small up to $\gamma = 7.1$ ” [12], i.e.
 2245 $G\gamma = 12.73$, $p = 6.6$ GeV/c; the table referred to stipulates a transition probability
 2246 $P_{\frac{1}{2}, -\frac{1}{2}} < 0.042$, whereas resonances beyond that energy range feature $P_{\frac{1}{2}, -\frac{1}{2}} > 0.36$.

³ Transition-gamma crossing, or “gamma jump”, is a common beam manipulation during acceleration in strong focusing synchrotrons, it requires an RF phase jump, the technique is addressed in Chapter 10.

2247 Beam depolarization up to 6 GeV/c, under the effect of these resonances, is illustrated
 2248 in Fig. 9.16.

2249 In a synchrotron using gradient dipoles, particles experience radial fields $B_x(y) =$
 2250 $-n \frac{B_0}{\rho_0} y$ as they undergo vertical betatron oscillations [12, 20, 21]. As n is small these
 2251 radial field components are weak, and so is their effect on spin motion.

Assuming a defect-free ring, the vertical betatron motion excites “intrinsic” spin resonances, located at

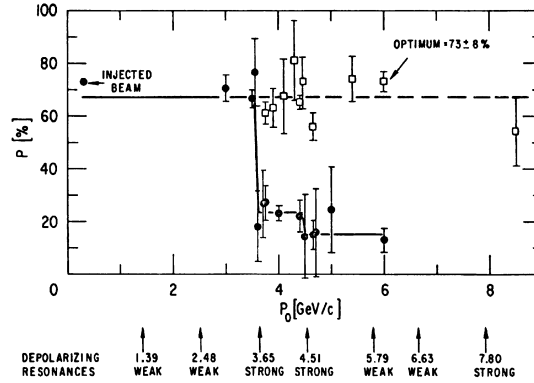
$$G\gamma_R = k P \pm \nu_y, \quad k \in \mathbb{N}$$

with P the period of the ring. In the ZGS for instance, $\nu_y \approx 0.8$ (Tab. 9.2), the ring is $P=4$ -periodic, thus $G\gamma_R = 4k \pm 0.8$. Strongest resonances are located at

$$G\gamma_R = mk P \pm \nu_y$$

2252 with m the number of cells per superperiod [22, Sec. 3.II]. In the ZGS, $m=2$ thus
 2253 strongest resonances occur at $G\gamma_R = 2 \times 4k \pm 0.8 = 7.2$ ($p = 3.65$ GeV/c), 8.8 (4.51 GeV/c), 15.2 (7.9 GeV/c), ... (Fig. 9.16).

Fig. 9.16 Polarization loss at the ZGS [23] through the strong intrinsic resonances $G\gamma_R = 7.2$ ($p = 3.65$ GeV/c) and 8.8 (4.51 GeV/c) (black circles). A tune jump method preserves polarization (empty circles)



2254 In the presence of vertical orbit defects, non-zero periodic transverse fields are experienced along the closed orbit, they excite “imperfection”, aka “integer”, depolarizing resonances, located at

$$G\gamma_R = k, \quad k \in \mathbb{N}$$

In the case of systematic defects the periodicity of the orbit is that of the lattice, P , imperfection resonances are located at $G\gamma_R = kP$. Strongest imperfection resonances are located at [22, Sec. 3.II]

$$G\gamma_R = mk P$$

2255 *Spin precession axis. Resonance width*

2256 Consider the spin vector $\mathbf{S}(\theta) = (S_\eta, S_\xi, S_y)$ of a particle in the laboratory frame,
 2257 with θ the orbital angle around the accelerator. Introduce the projection $s(\theta)$ of \mathbf{S} in
 2258 the median plane

$$s(\theta) = S_\eta(\theta) + jS_\xi(\theta) \quad (\text{and } S_y^2 = 1 - s^2) \quad (9.35)$$

2259 **Fig. 9.17** Modulus of the horizontal spin component. $s = 1/2$ at distance $\Delta = \pm\sqrt{3}\epsilon_R$ from $G\gamma_R$

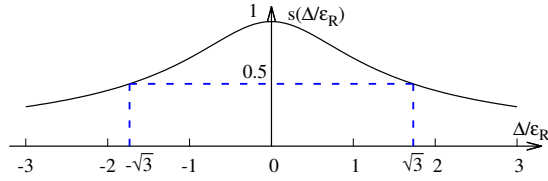
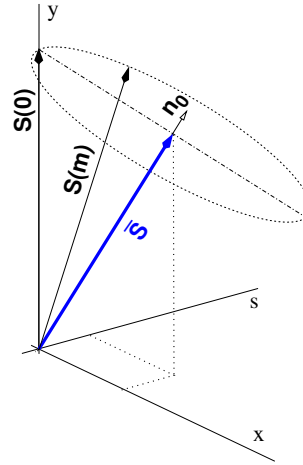


Fig. 9.18 Near an integer resonance, at any azimuth θ around the ring spins $\mathbf{S}(m)$ (m is the turn number, $\mathbf{S}(m)$ started vertical, here) precess at frequency $\omega = \sqrt{\Delta^2 + |\epsilon_R|^2}$ around a stationary axis $\mathbf{n}_0(\theta)$, whose orientation varies along the ring. \mathbf{n}_0 is aligned along $\bar{\mathbf{S}}$, average of $\mathbf{S}(m)$ over turns

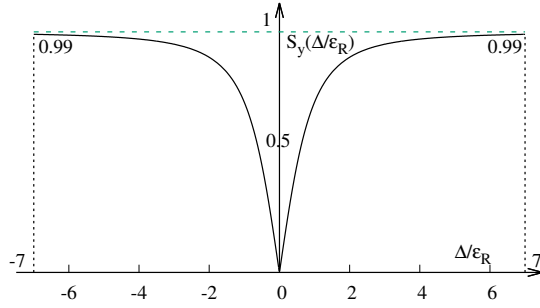


2260 In the case of a stationary solution of the spin motion, viz. stationary spin precession
 2261 axis around the ring (Fig. 9.18) [21, Sect. 3.6.1], s satisfies [21] (Fig. 9.17)

$$s^2 = \frac{1}{1 + \frac{\Delta^2}{|\epsilon_R|^2}} \quad (9.36)$$

2262 with $\Delta = G\gamma - G\gamma_R$ the distance to the resonance; thus the resonance width appears
 2263 to be a measure of its strength. The quantity of interest is the angle, ϕ , of the spin

Fig. 9.19 Dependence of polarization on the distance to the resonance. For instance $S_y = 0.99$, 1% depolarization, corresponds to $\Delta = \pm 7|\epsilon_R|$. On the resonance, $\Delta = 0$, the precession axis lies in the median plane, $S_y = 0$



2264 precession direction to the vertical axis, given by (Fig. 9.19)

$$\cos \phi(\Delta) \equiv S_y(\Delta) = \sqrt{1 - s^2} = \frac{\Delta/|\epsilon_R|}{\sqrt{1 + \Delta^2/|\epsilon_R|^2}} \quad (9.37)$$

2265 On the resonance, $\Delta = 0$, the spin precession axis lies in the bend plane: $\phi = \pm\pi/2$.
 2266 $S_y = 0.99$ (1% depolarization) corresponds to a distance to the resonance $\Delta = 7|\epsilon_R|$,
 2267 spin precession axis at an angle $\phi = \arccos(0.99) = 8^\circ$ from the vertical.

2268 Conversely, given S_y ,

$$\frac{\Delta^2}{|\epsilon_R|^2} = \frac{S_y^2}{1 - S_y^2} \quad (9.38)$$

The precession axis is common to all spins, S_y is a measure of the polarization along the vertical axis,

$$S_y = \frac{N^+ - N^-}{N^+ + N^-}$$

2269 wherein N^+ and N^- denote the number of particles in spin states $\frac{1}{2}$ and $-\frac{1}{2}$ respectively.
 2270

2271 Things complicate a little in the vicinity of an intrinsic resonance [21, Sect. 3.6.2],
 2272 the precession axis is not stationary, it precesses itself around the vertical, Fig. 9.20.

2273 *Resonance crossing*

2274 Crossing an isolated depolarizing resonance (Figs. 9.16, 9.21) causes a loss of
 2275 polarization given by the Froissart-Stora formula [24] [21, Sect. 2.3.6], ,

$$\frac{P_f}{P_i} = 2e^{-\frac{\pi}{2} \frac{|\epsilon_R|^2}{\alpha}} - 1 \quad (9.39)$$

2276 from a value P_i upstream to an asymptotic value P_f downstream of the resonance.
 2277 ϵ_R is the strength of the resonance [21, Sect. 2.3.5], and

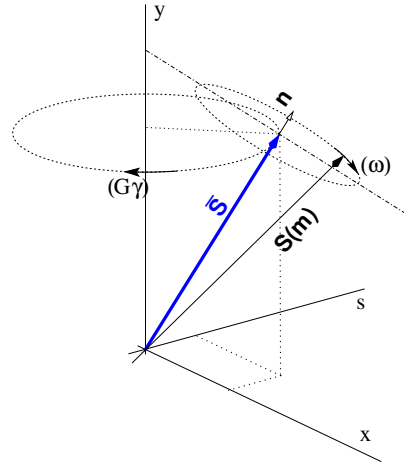


Fig. 9.20 Near an intrinsic resonance, spins $S(m)$ precess at frequency ω around an axis \mathbf{n} , which itself precesses around the vertical axis at frequency $G\gamma$

$$\alpha = G \frac{d\gamma}{d\theta} = \frac{1}{2\pi} \frac{\Delta E}{M} \tag{9.40}$$

2278 is the crossing speed for an energy gain ΔE per turn.

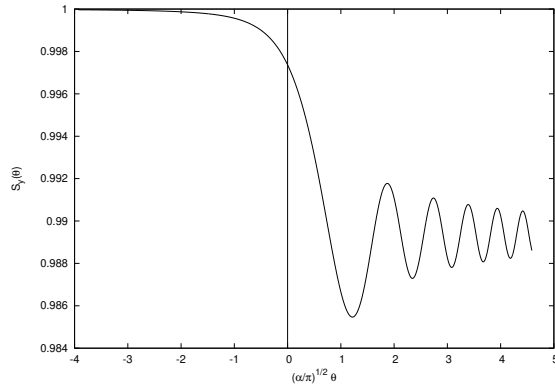


Fig. 9.21 Vertical component of spin motion $S_y(\theta)$ through a weak depolarizing resonance (Eq. 9.41). The vertical bar is at the location of the resonance, which coincides with the origin of the orbital angle

2279 *Spin motion through weak resonances*

Depolarizing resonances are weak up to several GeV in a weak focusing synchrotron, as the radial and/or longitudinal fields are weak. Thus assume $S_{y,f} \approx S_{y,i}$, with $S_{y,f}$ and $S_{y,i}$ the asymptotic vertical spin component values respectively upstream and downstream of the resonance; with the origin of the orbital angle taken at the resonance (Fig. 9.21), and introducing the Fresnel integrals [21]

$$C(x) = \int_0^x \cos\left(\frac{\pi}{2}t^2\right) dt, \quad S(x) = \int_0^x \sin\left(\frac{\pi}{2}t^2\right) dt$$

2280 the polarization satisfies

$$\begin{aligned} \text{if } \theta < 0 : \left(\frac{S_y(\theta)}{S_{y,i}}\right)^2 &= 1 - \frac{\pi|\epsilon_R|^2}{\alpha} \left\{ \left[\frac{1}{2} - C\left(-\theta\sqrt{\frac{\alpha}{\pi}}\right) \right]^2 + \left[\frac{1}{2} - S\left(-\theta\sqrt{\frac{\alpha}{\pi}}\right) \right]^2 \right\} \\ \text{if } \theta > 0 : \left(\frac{S_y(\theta)}{S_{y,i}}\right)^2 &= 1 - \frac{\pi|\epsilon_R|^2}{\alpha} \left\{ \left[\frac{1}{2} + C\left(\theta\sqrt{\frac{\alpha}{\pi}}\right) \right]^2 + \left[\frac{1}{2} + S\left(\theta\sqrt{\frac{\alpha}{\pi}}\right) \right]^2 \right\} \end{aligned} \quad (9.41)$$

2281 In the asymptotic limit,

$$\frac{S_y(\theta)}{S_{y,i}} \xrightarrow{\theta \rightarrow \infty} 1 - \frac{\pi}{\alpha} |\epsilon_R|^2 \quad (9.42)$$

2282 which identifies with the development of Froissart-Stora formula, Eq. 9.39, to the
2283 first order in $|\epsilon_R|^2/\alpha$. This approximation holds in the limit that higher order terms
2284 can be neglected: $|\epsilon_R|^2/\alpha \ll 1$.

2285 9.3 Exercises

2286 9.1 Construct SATURNE I (weak index) synchrotron. Spin Resonances

2287 Solution: page 313.

2288 In this exercise, the weak focusing 3 GeV synchrotron SATURNE I is modeled.
2289 Spin resonances in a weak dipole gradient lattice are observed.

Table 9.1 Parameters of SATURNE I weak focusing synchrotron [25]. ρ_0 denotes the reference bending radius in the dipole; the reference orbit, field index, wave numbers, etc., are taken along that radius

Orbit length, C	cm	6890
Average radius, $R = C/2\pi$	cm	1096.58
Drift length, $2l$	cm	400
Magnetic radius, ρ_0	cm	841.93
$R/\rho_0 = 1 + k$		1.30246
Field index n , nominal		0.6
Wave numbers ν_x, ν_y , nominal		0.72, 0.89
Stability limit		$0.5 < n < 0.757$
Injection energy (proton)	MeV	3.6
Field at injection	kG	0.326
Top energy	GeV	2.94
Field at top energy, B_{\max}	kG	14.9
\dot{B}	kG/s	18
Synchronous energy gain	keV/turn	1.160
RF harmonic		2

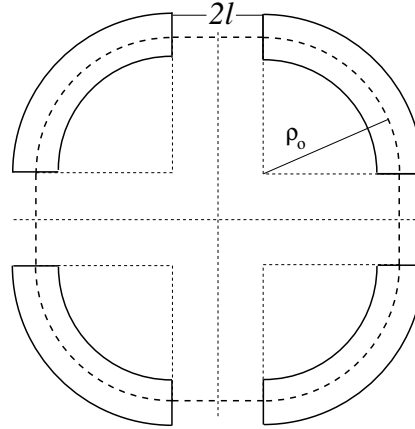


Fig. 9.22 A schematic layout of SATURNEI, a $2\pi/4$ axial symmetry structure, comprised of 4 radial field index 90 deg dipoles and 4 drift spaces. The cell in the simulation exercises is taken as a $\pi/2$ quadrant: half-drift/90°-dipole/half-drift

2290 (a) Construct a model of SATURNEI 90° cell dipole in the hard-edge model,
 2291 using DIPOLE. Use the parameters given in Tab. 9.1, and Fig. 9.22 as a guidance.
 2292 For beam monitoring purposes, split the dipole in two 45° deg halves. It is judicious
 2293 to take $RM=841.93$ cm in DIPOLE, as this is the reference radius for the definition
 2294 of the radial index. Take an integration step size in centimeter range - small enough
 2295 to ensure numerical convergence, as large as doable for fast multiturn raytracing.

2296 Validate the model by producing the 6×6 transport matrix of the cell dipole
 2297 (MATRIX[IFOC=0] can be used for that, with OBJET[KOBJ=5] to define a proper
 2298 set of paraxial initial coordinates) and checking against theory (Sect. 15.2, Eq. 15.6).

2299 (b) Construct a model of SATURNEI cell, with origin at the center of the drift.
 2300 Find the closed orbit, that particular trajectory which has all its coordinates zero in
 2301 the drifts: use DIPOLE[KPOS] to cancel the closed orbit coordinates at DIPOLE
 2302 ends. While there, check the expected value of the dispersion (Eq. 9.26) and of
 2303 the momentum compaction (Eq. 9.28), from the raytracing of a chromatic closed
 2304 orbit - *i.e.*, the orbit of an off-momentum particle. Plot these two orbits (on- and
 2305 off-momentum), over a complete turn around the ring, on a common graph.

2306 Compute the cell periodic optical functions and tunes, using either MA-
 2307 TRIX[IFOC=11] or TWISS; check their values against theory. Check consistency
 2308 with previous dispersion function and momentum compaction outcomes.

2309 Move the origin of the lattice at a different azimuth s along the cell: verify that,
 2310 while the transport matrix depends on the origin, its trace does not.

2311 Produce a graph of the optical functions (betatron functions and dispersion) along
 2312 the cell. Check the expected average values of the betatron functions (Eq. 9.20).

2313 Produce a scan of the tunes over the field index range $0.5 \leq n \leq 0.757$. RE-
 2314 BELOTE can be used to repeatedly change n over that range. Superimpose the
 2315 theoretical curves $\nu_x(n)$, $\nu_y(n)$.

(c) Justify considering the betatron oscillation as sinusoidal, namely,

$$y(\theta) = A \cos(\nu_y \theta + \phi)$$

2316 wherein $\theta = s/R$, $R = \oint ds/2\pi$.

2317 (d) Launch a few particles evenly distributed on a common paraxial horizontal
2318 Courant-Snyder invariant, vertical motion taken null (OBJET[KOBJ=8] can be used),
2319 for a single pass through the cell. Store particle data along the cell in zgoubi.plt,
2320 using DIPOLE[IL=2] and DRIFT[split,N=20,IL=2]. Use these to generate a graph
2321 of the beam envelopes.

2322 Using Eq. 9.22 compare with the results obtained in (b). Find the minimum
2323 and maximum values of the betatron functions, and their azimuth $s(\min[\beta_x])$,
2324 $s(\max[\beta_x])$. Check the latter against theory.

2325 Repeat for the vertical motion, taking $\varepsilon_x = 0$, ε_y paraxial.

2326 Repeat, using, instead of several particles on a common invariant, a single particle
2327 traced over a few tens of turns.

2328 (e) Produce an acceleration cycle from 3.6 MeV to 3 GeV, for a few particles
2329 launched on a common $10^{-4} \pi\text{m}$ initial invariant in each plane. Ignore synchrotron
2330 motion (CAVITE[IOPT=3] can be used in that case). Take a peak voltage $\hat{V} = 200 \text{ kV}$
2331 (unrealistic though, as it would result in a nonphysical \dot{B} (Eq. 9.29)) and synchronous
2332 phase $\phi_s = 150 \text{ deg}$ (justify $\phi_s > \pi/2$).

2333 Check the betatron damping over the acceleration range: compare with theory
2334 (Eq. 9.31).

2335 How close to symplectic the numerical integration is (it is by definition *not*
2336 symplectic, being a truncated Taylor series method [26, Eq. 1.2.4]), depends on the
2337 integration step size, and on the size of the flying mesh in the DIPOLE method [26,
2338 Fig. 20]; check a possible departure of the betatron damping from theory as a function
2339 of these parameters.

2340 Produce a graph of the horizontal and vertical wave number values over the
2341 acceleration cycle.

2342 (f) Some spin motion, now. Adding SPNTRK at the beginning of the sequence
2343 used in (e) will ensure spin tracking.

2344 Based on the input data file worked out for question (d), simulate the acceleration
2345 of a single particle, through the intrinsic resonance $G\gamma_R = 4 - \nu_y$, from a distance of
2346 a few times the resonance strength upstream (this requires determining BORO value
2347 under OBJET) to a distance of a few times the resonance strength downstream of the
2348 resonance, at an acceleration rate of 10 kV/turn.

2349 OBJET[KOBJ=8] can be used to allow to easily define an initial invariant value.

2350 Start with spin vertical. On a common graph, plot $S_y(\text{turn})$ for a few different
2351 values of the vertical betatron invariant (the horizontal invariant value does not
2352 matter - explain that statement, it can be taken zero). Derive the resonance strength
2353 from these tracking, check against theory.

2354 Repeat, for different crossing speeds.

2355 Push the tracking beyond $G\gamma = 2 \times 4 + \nu_y$: verify that the sole systematic resonances
2356 $G\gamma = \text{integer} \times P \pm \nu_y$ are excited - with $P = 4$ the periodicity of the ring.

2357 Break the 4-periodicity of the lattice by perturbing the index in one of the 4
2358 dipoles (say, by 10%), verify that all resonances $G\gamma = \text{integer} \pm \nu_y$ are now excited.

2359 (g) Consider a case of weak resonance crossing, single particle (*i.e.*, a case where
2360 $P_f/P_i \approx 1$, taken from (f)); crossing speed may be increased, or particle invariant

2361 decreased if needed), show that it satisfies Eq. 9.41. Match its turn-by-turn tracking
 2362 data to Eq. 9.41 so to get the vertical betatron tune ν_y , the location of the resonance
 2363 $G\gamma_R$, and its strength.

2364 (h) Stationary spin motion (*i.e.* at fixed energy) is considered in this question.
 2365 Track a few particles with distances from the resonance $\Delta = G\gamma - G\gamma_R = G\gamma - (4 - \nu_y)$
 2366 evenly spanning the interval $\Delta \in [0, 7 \times \epsilon_R]$.

2367 Produce on a common graph the spin motion $S_y(\text{turn})$ for these particles, as
 2368 observed at some azimuth along the ring.

Produce a graph of $\langle S_y \rangle|_{\text{turn}}(\Delta)$ (as in Fig. 9.19). Produce the vertical betatron
 tune ν_y , the location of the resonance $G\gamma_R$, and its strength, obtained from a match
 of $\langle S_y \rangle|_{\text{turn}}(\Delta)$ to (Eq. 9.37)

$$\langle S_y \rangle(\Delta) = \frac{\Delta}{\sqrt{|\epsilon_R|^2 + \Delta^2}}$$

2369 (i) Track a 200-particle 6-D bunch, with Gaussian transverse densities of $\epsilon_{x,y}$ a
 2370 few μm , and Gaussian $\delta p/p$ with $\sigma_{\delta p/p} = 10^{-4}$. Produce a graph of the average
 2371 value of S_y over a 200 particle set, as a function of $G\gamma$, across the $G\gamma_R = 4 - \nu_y$
 2372 resonance. Indicate on that graph the location of the resonant $G\gamma_R$ values.

2373 Perform this resonance crossing for five different values of the particle invariant:
 2374 $\epsilon_y/\pi = 2, 10, 20, 40, 200 \mu\text{m}$. Compute P_f/P_i in each case, check the dependence
 2375 on ϵ_y against theory.

2376 Compute the resonance strength, ϵ_y , from these tracking.

2377 Re-do this crossing simulation for a different crossing speed (take for instance
 2378 $\hat{V} = 10 \text{ kV}$) and a couple of vertical invariant values, compute P_f/P_i so obtained.
 2379 Check the crossing speed dependence of P_f/P_i against theory.

2380 9.2 Construct the ZGS (zero-gradient) synchrotron. Spin Resonances

2381 Solution: page 337.

2382 In this exercise, the ZGS 12 GeV synchrotron is modeled. Spin resonances in a
 2383 zero-gradient, wedge focusing synchrotron are studied.

2384 A photo taken in the ZGS tunnel is given in Fig. 9.4; a schematic layout of the ring
 2385 is shown in Fig. 9.23, and a sketch of the double dipole cell in Fig. 9.24. Table 9.2
 2386 details the parameters of the synchrotron resorted to in these simulations.

2387 (a) Construct a model of ZGS 45° cell dipole in the hard-edge model, using
 2388 DIPOLE. Use the parameters given in Tab. 9.2, and Figs. 9.23, 9.24 as a guidance.
 2389 For beam monitoring purposes, split the dipole in two 22.5° deg halves. Take the
 2390 closed orbit radius as the reference $RM=2076 \text{ cm}$ in DIPOLE: it will be assumed
 2391 that the orbit is the same at all energies⁴. Take an integration step size in centimeter
 2392 range - small enough to ensure numerical convergence, as large as doable for fast
 2393 multiturn raytracing.

2394 Validate the model by producing the 6×6 transport matrices of both dipole
 2395 (MATRIX[IFOC=0] can be used for that, with OBJET[KOBJ=5] to define a proper
 2396 set of paraxial initial coordinates) and checking against theory (Sect. 15.2, Eq. 15.6).

⁴ Note that in reality the reference orbit in ZGS moved outward during acceleration [27].

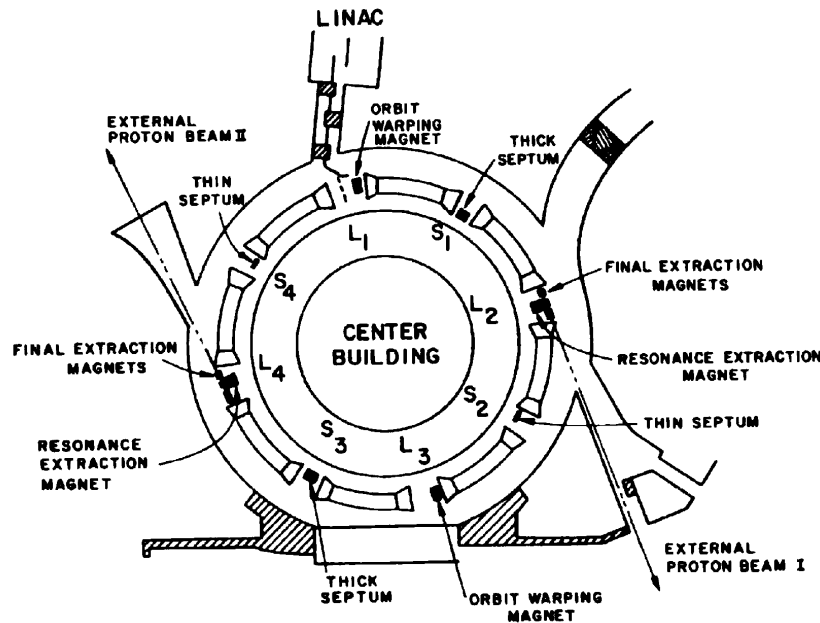


Fig. 9.23 A schematic layout of the ZGS [23], a $\pi/2$ -periodic structure, comprised of 8 zero-index dipoles, 4 long and 4 short straight sections

2397 Add fringe fields in `DIPOLE`[$\lambda, C_0 - C_5$], the rest of the exercise will use that
 2398 model. Take fringe field extent and coefficient values

$$\lambda = 60 \text{ cm } C_0 = 0.1455, C_1 = 2.2670, C_2 = -0.6395, C_3 = 1.1558, C_4 = C_5 = 0 \quad (9.43)$$

2399 ($C_0 - C_5$ determine the shape of the field fall-off, they have been computed from a
 2400 typical measured field profile $B(s)$).

2401 (b) Construct a model of ZGS cell accounting for dipole fringe fields, with origin
 2402 at the center of the long drift. In doing so, use `DIPOLE`[KPOS] to cancel the closed
 2403 orbit coordinates at DIPOLE ends.

2404 Compute the periodic optical functions at cell ends, and cell tunes, using `MA-`
 2405 `TRIX`[IFOC=11]; check their values against theory.

2406 Move the origin at the location (azimuth s along the cell) of the betatron functions
 2407 extrema: verify that, while the transport matrix depends on the origin, its trace does
 2408 not. Verify that the local betatron function extrema, and the dispersion function, have
 2409 the expected values.

2410 Produce a graph of the optical functions (betatron functions and dispersion) along
 2411 the cell.

2412 (c) Additional verifications regarding the model.

2413 Produce a graph of the field $B(s)$

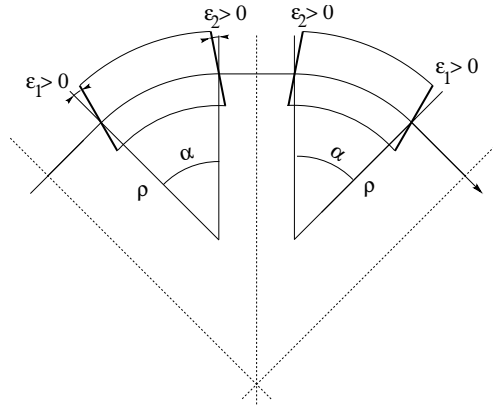


Fig. 9.24 A sketch of ZGS cell layout. In defining the entrance and exit faces (EFBs) of the magnet, beam goes from left to right. Wedge angles at the long straight sections (ε_1) and at the short straight sections (ε_2) are different

Table 9.2 Parameters of the ZGS weak focusing synchrotron after Refs. [27, 28] [23, pp. 288-294, p. 716] (2nd column, when they are known) and in the present simplified model and numerical simulations (3rd column). Note that the actual orbit moves during ZGS acceleration cycle, tunes change as well - this is not taken into account in the present modeling, for simplicity

		From Refs. [27, 28]	Simplified model
Injection energy	MeV		50
Top energy	GeV		12.5
$G\gamma$ span		1.888387 - 25.67781	
Length of central orbit	m	171.8	170.90457
Length of straight sections, total	m	41.45	40.44
<i>Lattice</i>			
Wave numbers $\nu_x; \nu_y$		0.82; 0.79	0.849; 0.771
Max. $\beta_x; \beta_y$	m		32.5; 37.1
<i>Magnet</i>			
Length	m	16.3	16.30486 (magnetic)
Magnetic radius	m	21.716	20.76
Field min.; max.	kG	0.482; 21.5	0.4986; 21.54
Field index			0
Yoke angular extent	deg	43.02590	45
Wedge angle	deg	≈ 10	13 and 8
<i>RF</i>			
Rev. frequency	MHz	0.55 - 1.75	0.551 - 1.751
RF harmonic $h = \omega_{rf} / \omega_{rev}$			8
Peak voltage	kV	20	200
B-dot, nominal/max.	T/s	2.15/2.6	
Energy gain, nominal/max.	keV/turn	8.3/10	100
Synchronous phase, nominal	deg		150
<i>Beam</i>			
$\varepsilon_x; \varepsilon_y$ (at injection)	$\pi \mu\text{m}$		25; 150
Momentum spread, rms			3×10^{-4}
Polarization at injection	%	> 75	100
Radial width of beam (90%), at inj.	inch	2.5	$\sqrt{\beta_x \varepsilon_x / \pi} = 1.1$

2414 - along the on-momentum closed orbit, and along off-momentum chromatic closed
 2415 orbits, across a cell;

2416 - along orbits at large horizontal excursion;

2417 - along orbits at large vertical excursion.

2418 For all these cases, verify qualitatively, from the graphs, that $B(s)$ appears as
 2419 expected.

(d) Justify considering the betatron oscillation as sinusoidal, namely,

$$y(\theta) = A \cos(\nu_y \theta + \phi)$$

2420 wherein $\theta = s/R$, $R = \oint ds/2\pi$.

2421 (e) Produce an acceleration cycle from 50 MeV to 17 GeV about, for a few particles
 2422 launched on a common $10^{-5} \pi\text{m}$ vertical initial invariant, with small horizontal
 2423 invariant. Ignore synchrotron motion (CAVITE[IOPT=3] can be used in that case).
 2424 Take a peak voltage $\hat{V} = 200 \text{ kV}$ (this is unrealistic but yields 10 times faster
 2425 computing than the actual $\hat{V} = 20 \text{ kV}$, Tab. 9.2) and synchronous phase $\phi_s = 150 \text{ deg}$
 2426 (justify $\phi_s > \pi/2$). Add spin, using SPNTRK, in view of the next question, (f).

2427 Check the accuracy of the betatron damping over the acceleration range, compared
 2428 to theory. How close to symplectic the numerical integration is (it is by definition
 2429 *not* symplectic), depends on the integration step size, and on the size of the flying
 2430 mesh in the DIPOLE method [26, Fig. 20]; check a possible departure of the betatron
 2431 damping from theory as a function of these parameters.

2432 Produce a graph of the evolution of the horizontal and vertical wave numbers
 2433 during the acceleration cycle.

2434 (f) Using the raytracing material developed in (e): produce a graph of the vertical
 2435 spin component of a few particles, and the average value over the 200 particle bunch,
 2436 as a function of $G\gamma$. Indicate on that graph the location of the resonant $G\gamma_R$ values.

2437 (g) Based on the simulation file used in (f), simulate the acceleration of a sin-
 2438 gle particle, through one particular intrinsic resonance, from a few thousand turns
 2439 upstream to a few thousand turns downstream.

2440 Perform this resonance crossing for different values of the particle invariant.
 2441 Determine the dependence of final/initial vertical spin component value, on the
 2442 invariant value; check against theory.

2443 Re-do this crossing simulation for a different crossing speed. Check the crossing
 2444 speed dependence of final/initial vertical spin component so obtained, against theory.

2445 (h) Introduce a vertical orbit defect in the ZGS ring.

2446 Find the closed orbit.

2447 Accelerate a particle launched on that closed orbit, from 50 MeV to 17 GeV about,
 2448 produce a graph of the vertical spin component.

2449 Select one particular resonance, reproduce the two methods of (g) to check the
 2450 location of the resonance at $G\gamma_R = \text{integer}$, and to find its strength.

2451 References

- 2452 1. Veksler, V.: A new method of acceleration of relativistic particles. J. of Phys. USSR 9 153-158
 2453 (1945)
- 2454 2. McMillan, E. M.: The Synchrotron. Phys. Rev. 68 143-144 (1945)
- 2455 3. Goward, F. K., and Barnes, D. E.: Experimental 8 MeV synchrotron for electron acceleration.
 2456 Nature 158, 413 (1946)
- 2457 4. Richardson, J.R., et al.: Frequency Modulated Cyclotron. Phys. Rev. 69: 669 (1946)
- 2458 5. Kerst, D. W.: The Acceleration of Electrons by Magnetic Induction.. Phys. Rev., 60, 47-53
 2459 (1941)
- 2460 6. SATURNE I photos: FAR_SA_N_00248, FAR_SA_N_02826; credit CEA Saclay. Archives
 2461 historiques CEA. Copyright CEA/Service de documentation
- 2462 7. Sessler, A., Wilson, E.: Engines of Discovery. A Century of Particle Accelerators. World
 2463 Scientific, 2007
- 2464 8. Fig. 9.3: Credit Reider Hahn, Fermilab
- 2465 9. Endo, K., et al.: Compact proton and carbon ion synchrotrons for radiation therapy. MOPRI087,
 2466 Proceedings of EPAC 2002, Paris, France; pp. 2733-2735.
 2467 <https://accelconf.web.cern.ch/e02/PAPERS/MOPRI087.pdf>
- 2468 10. Vostrikov, V.A., et al.: Novel approach to design of the compact proton synchrotron magnetic
 2469 lattice. tupsa17, 26th Russian Particle Accelerator Conference RUPAC2018, Protvino, Russia
 2470 (2018).
 2471 <https://accelconf.web.cern.ch/rupac2018/papers/tupsa17.pdf>
- 2472 11. Cohen, D. : Feasibility of Accelerating Polarized Protons with the Argonne ZGS. Review of
 2473 Scientific Instruments 33, 161 (1962).// <https://doi.org/10.1063/1.1746524>
- 2474 12. Ratner, L.G. and Khoe, T.K.: Acceleration of Polarized Protons in the Zero Gradient Syn-
 2475 chrotron. Procs. PAC 1973 Conference, Washington (1973).
 2476 http://accelconf.web.cern.ch/p73/PDF/PAC1973_0217.PDF
- 2477 13. Bywatwr, J., Khoe, T., et al.: A pulsed quadrupole system for preventing depolarization. IEEE
 2478 Transactions on Nuclear Science (Volume: 20, Issue: 3, June 1973)
- 2479 14. Cho, Y., et als.: Effects of depolarizing resonances on a circulating beam of polarized protons
 2480 during or storage in a synchrotron. IEEE Trans. Nuclear Science, Vol.NS-24, No.3, June 1977
- 2481 15. Parker, E.F.: High Energy Polarized Deuterons at the Argonne National Laboratory Zero
 2482 Gradient Synchrotron. IEEE Transactions on Nuclear Science, Vol. NS-26, No. 3, June 1979,
 2483 pp 3200-3202

- 2484 16. Suddeth, D.E., et als.: Pole face winding equipment for eddy current correction at the Zero
2485 Gradient Synchrotron. Procs. PAC 1973 Conference, Washington (1973).
2486 http://accelconf.web.cern.ch/p73/PDF/PAC1973_0397.PDF
- 2487 17. Rauchas, A.V. and Wright, A.J.: Betatron tune profile control in the Zero Gradient Synchrotron
2488 (ZGS) using the main magnet pole face windings. Procs. PAC1977 conference, IEEE Trans.
2489 on Nucl. Science, VoL.NS-24, No.3, June 1977
- 2490 18. Floquet, G.: Sur les équations différentielles linéaires à coefficients périodiques. Annales
2491 scientifiques de l'E.N.S. 2e série, tome 12 (1883), p. 47-88.
2492 http://www.numdam.org/item?id=ASENS_1883_2_12_47_0
- 2493 19. Leleux, G.: Accélérateurs Circulaires. Lecture Notes, INSTN, CEA Saclay (1978)
- 2494 20. Leleux, G.: Traversée des résonances de dépolarisation. Rapport Interne LNS/GT-91-15,
2495 SATURNE, Groupe Théorie, CEA Saclay (février 1991)
- 2496 21. Méot, F.: Spin Dynamics. In: Polarized Beam Dynamics and Instrumentation in Particle
2497 Accelerators, USPAS Summer 2021 Spin Class Lectures, Springer Nature, Open Access (2023).
2498 <https://link.springer.com/book/10.1007/978-3-031-16715-7>
- 2499 22. Lee, S.Y.: Spin Dynamics and Snakes in Synchrotrons. World Scientific, 1997
- 2500 23. Khoe, T.K., et al.: The High Energy Polarized Beam at the ZGS. Procs. IXth Int. Conf on
2501 High Energy Accelerators, Dubna, pp. 288-294 (1974).
2502 Fig. 9.16: Copyrights under license CC-BY-3.0, <https://creativecommons.org/licenses/by/3.0/>;
2503 no change to the material
- 2504 24. Froissart, M. and Stora, R.: Dépolarisation d'un faisceau de protons polarisés dans un syn-
2505 chrotron. Nucl. Inst. Meth. 7 (1960) 297.
- 2506 25. Bruck H., Debraine P., Levy-Mandel R., Lutz J., Podliasky I., Prevot F., Taieb J., Winter S.D.,
2507 Maillet R., Caractéristiques principales du Synchrotron des Protons de Saclay et résultats
2508 obtenus lors de la mise en route, rapport CEA no.93, CEN-Saclay, 1958.
- 2509 26. Méot, F.: Zgoubi Users' Guide.
2510 <https://www.osti.gov/biblio/1062013-zgoubi-users-guide> Sourceforge latest version:
2511 <https://sourceforge.net/p/zgoubi/code/HEAD/tree/trunk/guide/Zgoubi.pdf>
- 2512 27. Foss, M.H., et al.: The Argonne ZGS Magnet. IEEE 1965, pp. 377-382, June 1965
- 2513 28. Klaisner, L.A., et al.: IEEE 1965, pp. 133-137, June 1965